

# ANALYSIS OF THREE-DIMENSIONAL WOVEN COMPOSITES

M. Keith Ballard<sup>1</sup>, J. Scott McQuien<sup>2</sup> and John D. Whitcomb<sup>3</sup>

<sup>1</sup> Texas A&M University, Department of Aerospace Engineering, [kballard@tamu.edu](mailto:kballard@tamu.edu)

<sup>2</sup> Texas A&M University, Department of Aerospace Engineering, [smcquien@gmail.com](mailto:smcquien@gmail.com)

<sup>3</sup> Texas A&M University, Department of Aerospace Engineering, [jdwt@tamu.edu](mailto:jdwt@tamu.edu)

**Keywords:** Three-dimensional woven textile composite, Finite element analysis

## ABSTRACT

Three finite element meshes with increasing refinement, ranging from 62k to 2 million nodes, were created for a 3D orthogonally interlocked composite textile based on geometry generated by VTMS. Each mesh was subjected to uniaxial extension in the plane of the textile, and the stresses predicted by each of the three meshes were used to understand the convergence and stress distributions within each constituent. The coarse model predicted volume average stresses within 22% of those predicted by the refined model, while the model with a medium refinement predicted values within 7%. The most severe stress component within each type of tow was investigated. The transverse normal stress  $\sigma_{yy}^M$  in the y-direction tows was the most severe, which indicates that matrix cracking within the y-direction tows perpendicular to the applied load is most likely to occur before failure in other tows. For the severe stress components, the maximum stress in the material increased with increasing mesh refinement. The models seemed to be converging, but it is unclear if even the refined model reached an acceptable level of convergence. However, even if convergence is achieved, the very small volumes of material at high stress levels might require consideration of the heterogeneous microstructure in order to accurately predict the stresses and initiation of damage in critical regions.

## 1 INTRODUCTION

Textile composites have been routinely used within the aerospace industry, but often designs are limited to two-dimensional weaves because of the difficulty in characterizing and manufacturing three-dimensional weaves. Woven textiles offer increased toughness and out of plane properties compared to laminated composites composed of unidirectional plies. Three-dimensional woven textiles use through thickness tows that tie the layers together, which can improve out of plane properties and significantly improves impact resistance over 2D woven textiles. Three-dimensional woven composites have been used for some applications, such as blade containment systems and body armor, and they offer the potential for multifunctional applications, such as integrating active cooling, self-healing, or a tunable antenna into the material. [1] [2] [3] [4] Predicting even the elastic stress distributions in 3D woven composites poses several challenges, including modelling realistic tow geometries, creating a valid finite element mesh, and solving large systems of equations. Some researchers have successfully created models for a unit cell of a 3D woven composite, but the complex geometry, large mesh, and difficult computational challenges result in relatively few works in the literature on the topic. [5] [6] [7] In 2012, Drach et. al. used a tool called DFMA, which is very similar to the one used in this study, to create a realistic unit cell for 3D textiles [5], and that model was later used for a few other studies. [8] However, a detailed look at distribution of stresses within the material using a realistic model like the one used in Ref. [5] was never done. Some groups have used non-standard FEA models, but the accuracy of such models has not been well-characterized. One such example is the voxel approach used by Green et. al. [6] As researchers continue to analyze 3D woven composites, it becomes important to characterize mesh convergence for such complex geometries and understand the effect of textile geometry on local stress concentrations, but this topic has received little attention. This paper explores the mesh convergence behavior and stress states within a 3D orthogonally interlocked woven textile model with realistic tow geometry.

This paper is separated into two primary sections. The first section describes the model, material properties, and boundary conditions for this study. This is followed by the results section, which describes the general convergence behavior of the three meshes and the distributions of stress within the constituents. Within the results section, the volume average stresses are investigated, followed by a section on the most severe component of stress for each type of tow.

## 2 FINITE ELEMENT MODEL

This section describes the finite element analysis (FEA) model, including the mesh, the material properties assumed for each constituent, and the boundary conditions considered in this paper.

### 2.1 Geometry and Meshes

A software tool called VTMS was used to create realistic geometry for a 3D orthogonal weave. The geometry used for this study is shown in Figure 1. The Air Force Research Lab (AFRL) developed VTMS for modeling the effects of processing on the tow geometry, allowing the generation of realistic textile models. The VTMS software includes meshing for the independent mesh method [9], but this functionality was not used. Instead, this work will use a standard FEA formulation, requiring a conforming mesh. Using an in-house tool, the tow surface geometries were extracted from VTMS and used with a general tetrahedral meshing tool, TetGen [10], to create a conforming quadratic tetrahedral mesh for the tows and matrix. Within VTMS, the refinement of the surface geometry of the tows can be controlled by specifying the number of stacks and slices. However, the surface geometry information that is taken from VTMS is faceted, resulting in unrealistic sharp corners between facets. The in-house tool used the average size of the tow surface elements from VTMS to control the size of the elements. To investigate the convergence of the model, the same geometry was used within VTMS to generate a sequence of three increasingly refined surface geometries, and from those surface geometries, a sequence of three increasingly refined FEA meshes were generated. Some information about the sequence of meshes is shown in Table 1. It should be noted that because of the complex geometry, as the surface geometry from VTMS is refined the volume of the tows change, which is why the tow volume fraction changes for the meshes in Table 1. Figure 2 shows the sequence of meshes used in this paper. As Figure 2 shows, the element size within the mesh was not uniform, with higher refinement existing near the boundaries of constituents.

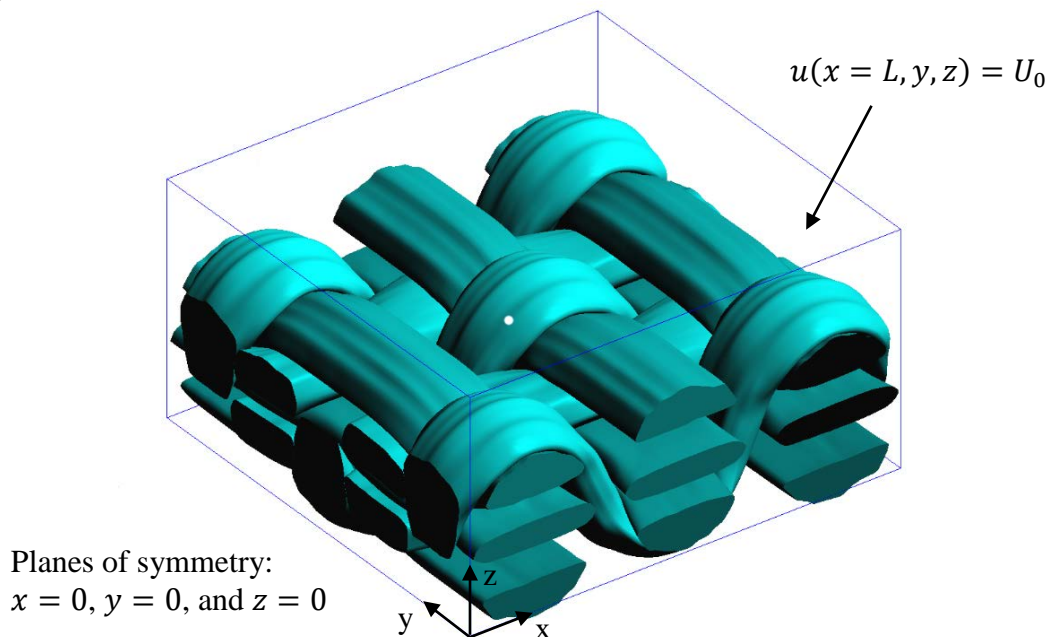


Figure 1. Illustration of geometry in VTMS and applied boundary conditions

Mesh	# Nodes	# Elements	Tow Volume Fraction
Coarse	61,906	42,306	53.9%
Medium	374,473	266,129	56.1%
Refined	1,962,148	1,436,552	56.7%

Table 1. Basic mesh statistics meshes used for the study

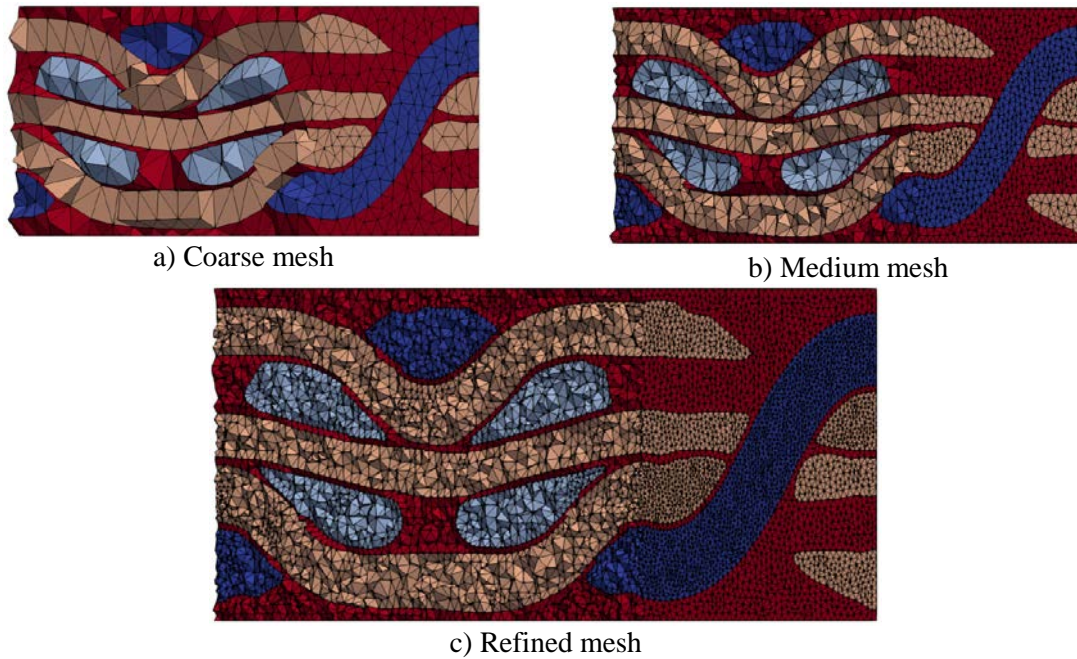


Figure 2. Clipped region of unit cell showing the different mesh refinements

## 2.2 Material Properties

The material properties for both constituents were taken from Ref. [11], which used an analytical homogenization scheme to predict the properties of the tows based on the measured properties of the matrix and graphite fibers. The matrix was assumed to be isotropic with the values:  $E = 2.9 \text{ GPa}$  and  $\nu = 0.3$ . The tows were assumed to be homogenous and transversely isotropic with the values:  $E_{11} = 221.4 \text{ GPa}$ ,  $E_{22} = E_{33} = 12.6 \text{ GPa}$ ,  $G_{12} = G_{13} = 7.4 \text{ GPa}$ ,  $\nu_{12} = \nu_{13} = 0.34$ , and  $\nu_{23} = 0.32$ . Since this is an initial study into the convergence behavior and stress distributions of 3D textile models, linear elasticity was assumed.

## 3.3 Boundary Conditions

Ideally, periodic boundary conditions would be used on the textile unit-cell, but the geometry from VTMS is not periodic, making it impossible to accurately enforce periodicity. Three faces of the unit cell (the  $x = 0$ ,  $y = 0$ , and  $z = 0$  planes) were assumed to be planes of symmetry, refer to Figure 1. This resulted in the following boundary conditions:  $u(x = 0, y, z) = 0$ ,  $v(x, y = 0, z) = 0$ , and  $w(x, y, z = 0) = 0$ . The x-direction displacement on the  $x = L$  face of the unit cell was specified such that the unit cell experienced 1% strain, where  $L$  is the in-plane dimension of the unit-cell.

## 4 RESULTS

This section describes the convergence behavior and stress distributions for a 3D textile unit cell

under uniaxial extension. The results are separated into four sections. The first section investigates the volume average stresses within each type of tow. Next, a section discuss the most severe component of stresses in each of the types of tows: orthogonal tows, x-direction tows, and y-direction tows.

#### 4.1 Volume Average Stresses

The volume average stresses within each constituent provide an initial measure of mesh convergence and insight into how load is transferred within the textile. Table 2 shows each component of the volume average stresses in the material coordinate system within each constituent for the refined mesh. The superscript “M” indicates that the stresses are in the material coordinate system. For the two coarser meshes, the percent difference from the volume average stress of the refined mesh is shown.

Table 2 can be used to understand the convergence of the three meshes, but it should be noted that the convergence includes convergence of geometry as well as mesh refinement. The geometry changes with increasing mesh refinement to capture the tow geometry modeled within VTMS more accurately. Unfortunately, for this paper, there was no method implemented for separating these two effects.

For the normal stress along the fiber direction, the coarse mesh predicted a volume average value within 5% for the orthogonal and x-direction tows, which are both nominally along the direction of the applied load. The y-direction tows experience a compressive stress in the fiber direction since they run transverse to the applied load and oppose the Poisson contraction of the unit cell. For this stress component, the coarse mesh predicted a volume average stress that was 22% larger than the value predicted by the refined mesh. For the transverse normal stresses,  $\sigma_{yy}^M$  and  $\sigma_{zz}^M$ , within each tow, the medium and coarse mesh predicted a volume stress that was close to the value predicted by the refined mesh, remaining within 7%. For the shear stresses, the refined mesh generally predicted more severe volume average stresses than the two coarser meshes. The coarse mesh predicted a value up to 16.8% lower than the value predicted by the refined mesh, while the medium mesh performed well, predicting the volume average shear stress within 7%.

Overall, the coarse mesh predicted volume average stresses within 20% of the refined mesh, while the medium mesh predicted a volume average stress within 7% of the refined mesh. Although the predictions appear to be converging, the refined mesh cannot be said to be converged, and even more refined meshes are needed to determine the converged values precisely.

Constituent	Mesh	$\langle \sigma_{xx}^M \rangle$	$\langle \sigma_{yy}^M \rangle$	$\langle \sigma_{zz}^M \rangle$	$\langle  \sigma_{xy}^M  \rangle^*$	$\langle  \sigma_{yz}^M  \rangle^*$	$\langle  \sigma_{xz}^M  \rangle^*$
Orthogonal Tows	Coarse	-0.9%	-7.0%	-3.5%	-16.8%	-2.7%	-5.0%
	Medium	0.4%	-5.8%	-0.6%	-7.0%	0.3%	-0.9%
	Refined	2.29e8	-3.62e6	2.98e7	5.17e6	7.99e6	4.43e7
X-Direction Tows	Coarse	4.9%	-1.3%	4.0%	-5.5%	-12.8%	-3.4%
	Medium	1.2%	-0.3%	2.1%	-1.7%	-2.8%	-1.0%
	Refined	-0.9%	-7.0%	-3.5%	-16.8%	-2.7%	-5.0%
Y-Direction Tows	Coarse	21.7%	-3.5%	-3.0%	-12.2%	-9.3%	1.5%
	Medium	7.0%	-0.6%	0.9%	-3.6%	-3.5%	-1.4%
	Refined	-1.19e7	7.77e7	-2.09e7	5.63e6	3.82e6	1.12e7

\* Note: volume average shear stresses were calculated using the absolute value of the stress, since the volume average shear stress would be close to zero.

Table 2. Volume average stresses (in the material coordinate system) in each constituent for the different meshes

In addition to convergence, the volume average stresses shown in Table 2 indicate how load is transferred within the textile. Since the x-direction tows are aligned with the load direction, they experience the highest level of stress, as expected. In the material coordinate system of the x-direction tows, the local z-axis generally aligns with the global z-axis, which is out of plane of the textile. Consequently, the local x- and y-axes generally align within the plane of the textile. Table 3 shows that the x-direction tows experience tension in the two in-plane directions and compression out of plane. In the x-direction tows, the fibers align with the applied load, so the tension along the local x-axis is expected. Regarding the tension within the x-direction tows in the direction transverse to the fibers and

in the plane of the textile (local y-axis), the unit cell contracts due to the Poisson effect, but the y-direction tows are stiffer than the other constituents in the transverse in-plane direction and have a smaller Poisson's ratio. Consequently, the y-direction tows experiences compression while the x-direction tows experience tension. The compression in the out of plane direction is due to the orthogonal tows trying to straighten due to the applied extensional load in the direction of the orthogonal tow undulation. The orthogonal tows interlock with the y-direction tows and compress the x-direction and y-direction tows, while the orthogonal tow experiences a tensile stress out of plane. This was confirmed by calculating the volume average stress within the orthogonal tows in the global z-direction, which was indeed tensile. Additionally, in a study not shown in this paper, the orthogonal tows were replaced by matrix. For that case, the x-direction tows experience tension instead of compression in the out of plane direction, indicating it is the orthogonal tows trying to straighten that leads to the compressive stresses in the x-direction tows. It is important to remember that the volume average stress in the entire unit cell is zero except in the direction of the applied load.

Additionally, the x-direction tows experience relatively severe shear stresses in every component. Since the x-direction tows are carrying most of the load in the direction of the applied load and matrix pockets exist in regions of the textile, the load is often distributed to the neighboring tows through shear stresses.

Since the y-direction tows lie transverse to the direction of the applied load, they experience a relatively high transverse normal stress,  $\sigma_{yy}^M$ . The compressive stresses for the other two normal components were discussed earlier. Of the three types of tows, the y-direction tows generally experienced a less severe volume average shear stress, except for one component,  $\sigma_{xz}^M$ . Compared to the orthogonal tows, the y-direction tows did experience a slightly higher  $\langle \sigma_{xy}^M \rangle$ . Since there are matrix regions between the tows, load is transferred from the x-direction tows and orthogonal tows to the y-direction tows via this component of shear stress, which is the in-plane shear stress component for the textile for the y-direction tows.

## 4.2 Stress Distribution within Tows

This section investigates the stress distribution of the most severe stress component each within each type of tow. Though accurate strengths are not available for the material system assumed in this paper, the magnitude of each strength relative to the other strengths for a different tow material can be assumed to be representative for this material. The strengths used in Ref. [6] were used to understand which stress components might be the most severe. The strengths will not be used herein to predict failure, but rather, they will only be used to select the most severe stress component to investigate for each type of tow. To select the most severe component of stress, the maximum value for each component of stress was compared against a scaled allowable stress.

### 4.2.1 Orthogonal Tows

For the orthogonal tows, the normal stress along the z-axis in the material coordinate system,  $\sigma_{zz}^M$ , was clearly the most severe component of stress. Figure 3 shows the percentage of the constituent within various stress ranges for each of the mesh refinements. From the column plot in Figure 3, even the coarsest mesh (green bars) captures the amount of material at relatively low stresses well. However, it poorly predicts the material at severe tensile and compressive stresses. The orthogonal tows experience a tensile  $\sigma_{zz}^M$  on average, as shown in the figure and Table 2, but locally, the stress varies from severe compressive to severe tensile stresses. In the contour plots in Figure 3 and subsequent figures, the color mapping is centered on the volume average stress within the constituent, which means that shades of red indicate a stress larger than the volume average, shades of blue indicate a stress lower than the volume average, and gray indicates a stress near the volume average. The orthogonal tows experience compression where they cross over or under a y-direction tow, very near the area of contact between the two tows. A typical location is labeled A in Figure 3. Compressive stresses develop in these regions because the orthogonal tows want to straighten out but are resisted by the y-direction tows. Consequently, compressive stresses form where the orthogonal tow presses against the y-direction tows.

However, within the matrix rich region that lies between the rows of y-direction tows, the orthogonal tows generally experience a tensile  $\sigma_{zz}^M$ , as shown in region B of Figure 3. In these regions, the local z-axis has a significant component along the global x-axis, which is the direction of the applied tensile load. Therefore, the orthogonal tows experience a tensile  $\sigma_{zz}^M$  in these matrix rich regions.

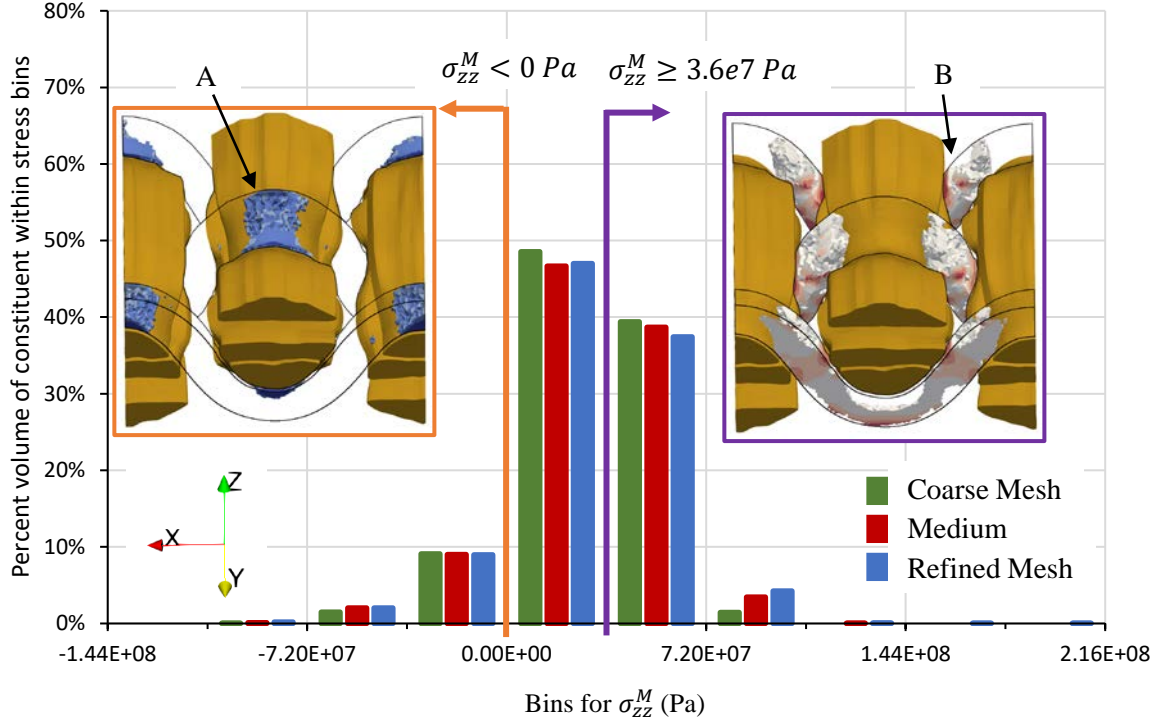


Figure 3. Distribution of  $\sigma_{zz}^M$  within orthogonal tows for the different mesh refinements with images showing material below 0 Pa or above 3.6e7 Pa. For the contour plots, gray indicates a stress near the volume average in the constituent, while red and blue indicates a stress higher or lower respectively.

Figure 3 focused on the entire distribution of  $\sigma_{zz}^M$ , but the highest stresses are of critical importance to understand where damage might initiate. A large tensile  $\sigma_{zz}^M$  tends to lead to matrix cracks within the tow. Because of this concern, it is important to consider the highest stresses. Figure 4 shows the stress distribution and locations of the material within the tow with a  $\sigma_{zz}^M$  higher than  $8e7$  Pa. Data labels are shown for the refined mesh, since the volume percentage in the last seven bins are difficult to compare due to the very small values. Concerning convergence, the coarse mesh does a very poor job at predicting any material at these high stress levels and only predicted that the stress level of the first bin is reached. The medium mesh somewhat captures the stress distribution for the first two to four bins, but it fails to predict any material reaches the stress levels of the last five bins. As expected, increasing mesh refinement seems to be headed towards convergence, but even further mesh refinement is needed to know if the converged maximum stress is reached with the refined mesh used in this study. The location of the highest  $\sigma_{zz}^M$  in the orthogonal tows is of interest since damage is likely to initiate at those concentrations. The contour plot in Figure 4 shows the material within all the bins shown in Figure 4. The highest values generally exist in the matrix rich regions between rows of y-direction tows but also close to the edge of the matrix rich regions, near the y-direction tows themselves, as shown in the contour plot in Figure 4. However, many of the locations of high stresses also lie near relatively sharp edges of the tow. Because of the nature of the geometry generation algorithm in VTMS, each tow's surface geometry is faceted, not smooth. These artifacts can cause higher stresses where the facets form sharp edges. This topic requires further study to know if approximations in the model are strongly influencing the highest stress concentrations. Additionally, the smallest stress concentration regions can fit within a sphere that has a diameter that is  $1/100^{\text{th}}$  of a tow thickness or less, which is much less than a fiber diameter. Even if the model converges at a higher refinement, at that scale, the heterogeneous microstructure of the tow would need to be considered.

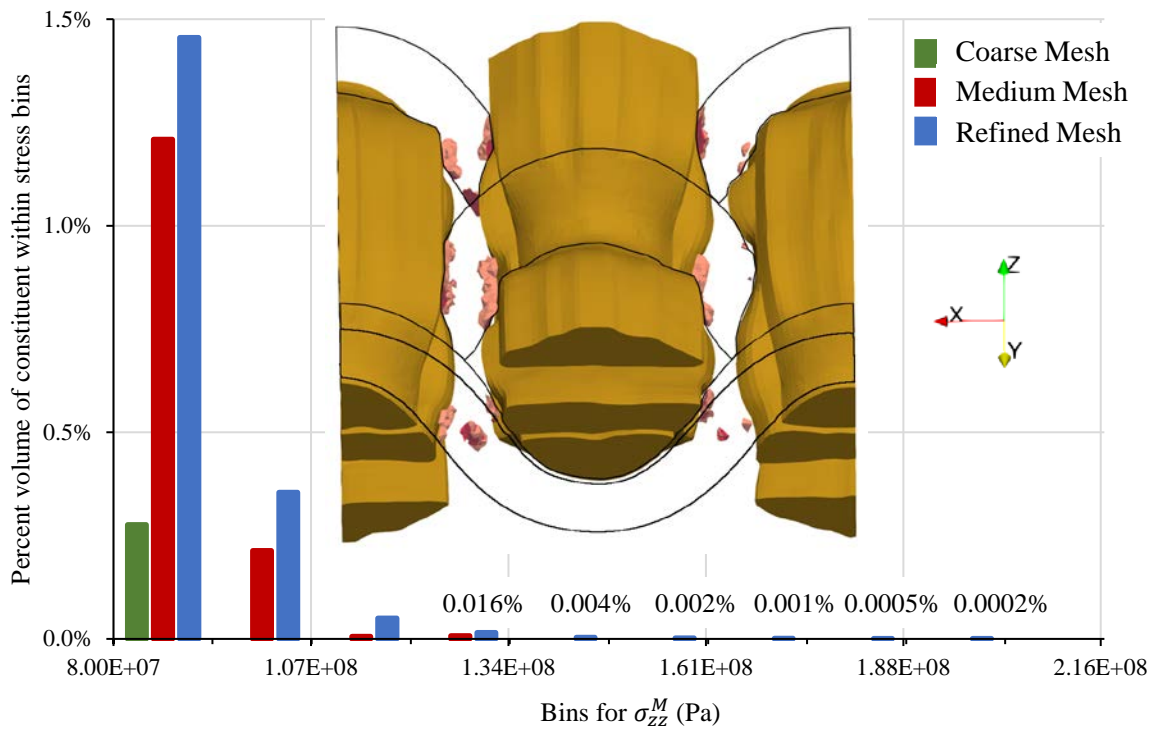


Figure 4. Distribution of  $\sigma_{zz}^M$  at high stress levels within the orthogonal tows for the different mesh refinements with an image showing material above  $8e7$  Pa. In the contour plot, red indicates a stress greater than the volume average.

#### 4.2.2 X-Direction Tows

Using the same methodology as described in the beginning of the previous section, the longitudinal shear stress was selected as the most severe stress component for the x-direction tows. The magnitude of the stress along the fiber direction was very high, but the tensile strength of tows along the fiber direction is often at least an order of magnitude greater than the shear and transverse tensile strengths. Of the different types of tows, the x-direction tows experiences stress that were least severe compared to the scaled allowables, which are just used for comparison.

The entire stress by volume histogram is not shown here, but data showed that all three meshes predicted very similar distributions for low levels of stress. However, the high stresses are of much greater interest. Since this paper is concerned with the severity of the shear stress, the sign is not important for this discussion, so the absolute value of the shear stresses will be shown. Figure 5 shows the percentage of the x-direction tow that reach stresses larger than  $1.76e8$  Pa. A relatively large range of stresses is shown in Figure 5, and since the coarser mesh under predicts the amount of volume at the very high stresses, it over predicts the amount of material at a lower stress, represented by the first bin. The coarse mesh poorly predicts the stress distribution for the last eight bins. The medium mesh seems to capture the trend well until the last three or four bins. As with  $\sigma_{zz}^M$  in the orthogonal tows, the maximum stress in the constituent continues to increase as the mesh is refined. It is unclear if the refined model has reached sufficient convergence.

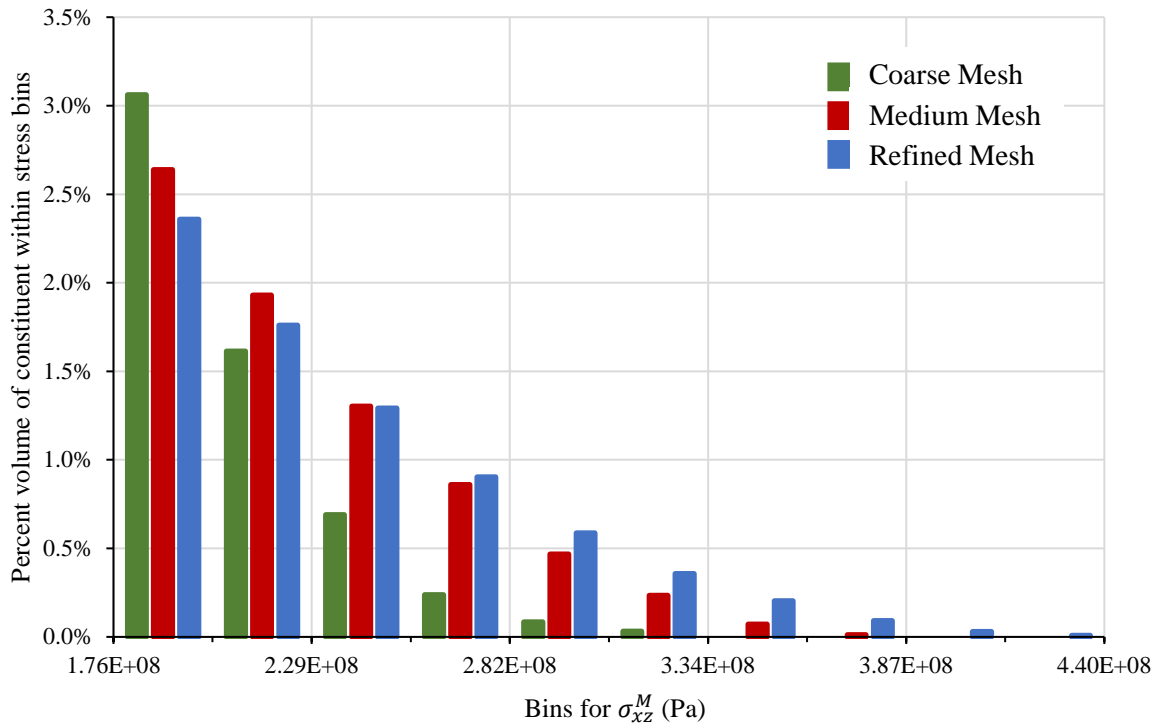


Figure 5. Distribution of  $\sigma_{xz}^M$  at high stresses within the x-direction tows for different mesh refinements

The location of the high shear stresses provide insight into where damage might occur within the x-direction tows, though an accurate location of damage initiation cannot be determined without a progressive failure analysis since damage in other constituents will affect the stress distribution in this constituent. Figure 6 shows contours for the portion of x-direction tows with magnitudes of  $\sigma_{xz}^M$  higher than  $8e7$  Pa, which includes a wider range of stresses than what is shown in the histogram of Figure 5. Since the x-direction tows generally align with the global coordinate system, the local x-axis is generally along the loading direction and the local z-axis is generally out of plane. Considering this, it seems that load is being transferred in the matrix rich regions to the neighboring orthogonal tows, which have their greatest out of plane component in the same regions, since the concentrations all remain close to the area where the orthogonal tows cross the x-direction tow paths, as shown in Figure 6a. Additionally, the shear stress concentrations are generally closer to the midplane of the unit cell, as shown in Figures 6c and 6d. However, the high stress seems very localized to the outermost region of the tow, as shown in Figure 6c.

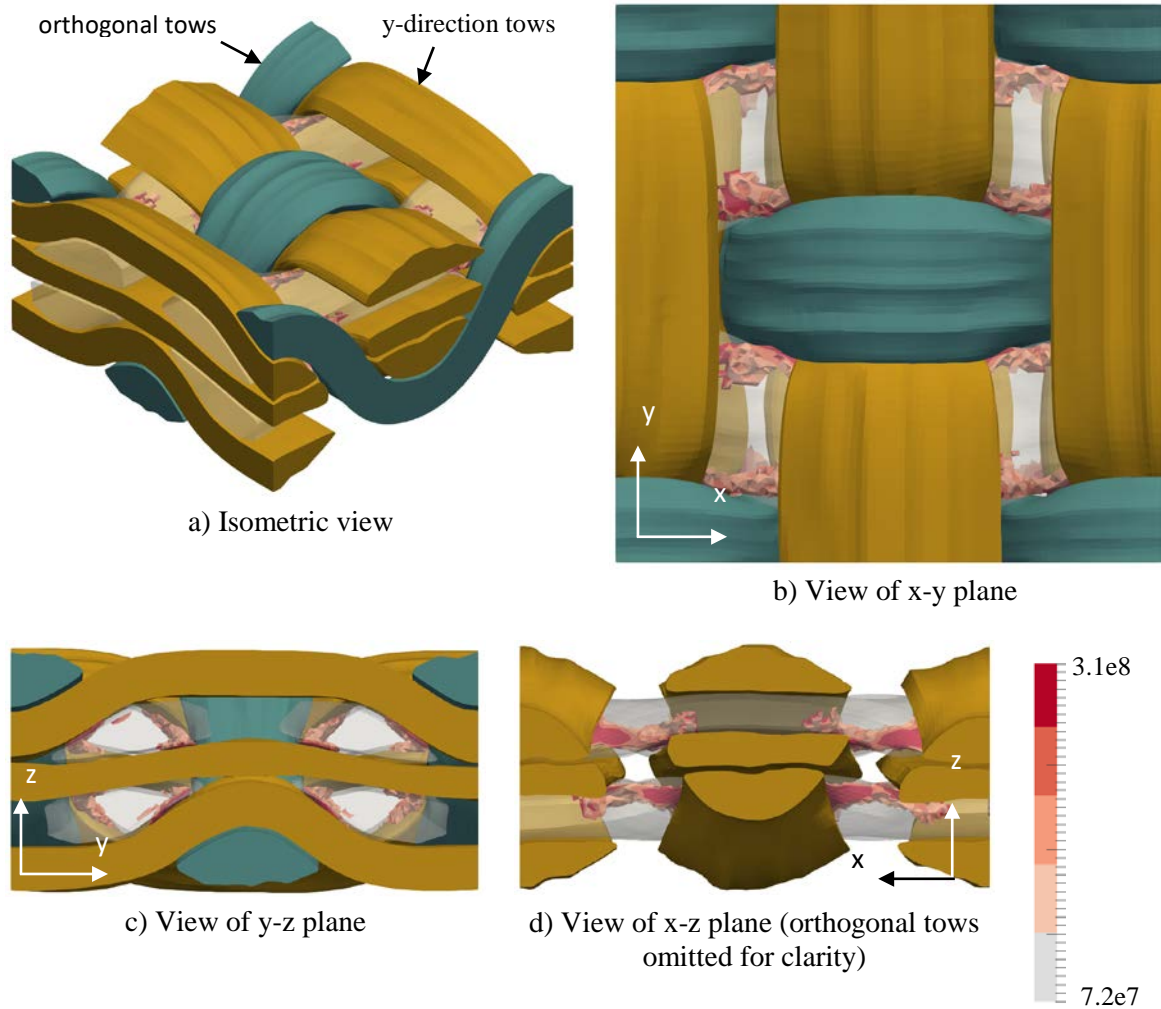


Figure 6.  $\sigma_{xz}^M$  contours for regions of the x-direction tows with  $abs(\sigma_{xz}^M) > 8e7 Pa$ . Orthogonal and y-direction tows are shown for context. The entire x-direction tows are also overlaid as a semi-transparent gray solid.

#### 4.2.3 Y-Direction Tows

Since the fibers run transverse to the applied load for the y-direction tows, the transverse normal stress  $\sigma_{yy}^M$  for the y-direction tows reached high values, and the allowable for this component of stress will be significantly less than the allowable in the direction of the fibers. Consequently,  $\sigma_{yy}^M$  was the most severe of all the stresses within any type of tow by a large margin.

Figure 7 shows a histogram of the amount of material in the y-direction tows within various bins of values for  $\sigma_{yy}^M$ . A significant percentage of the material experiences relatively high tensile stresses; however, the tows do not carry that load evenly. The middle layer of y-direction tows carries substantially more of the load than the top and bottom layers, as shown in Figure 7b. This is due to the middle layer of y-direction tows being surrounded by two layers of x-direction tows, which are carrying most of the load within the textile for the applied load considered in this paper. Whereas, the top and bottom layers of y-direction tows have less avenues for load to be transferred to them with only one nearby layer of x-direction tows, and thereby experience lower transverse normal stresses.

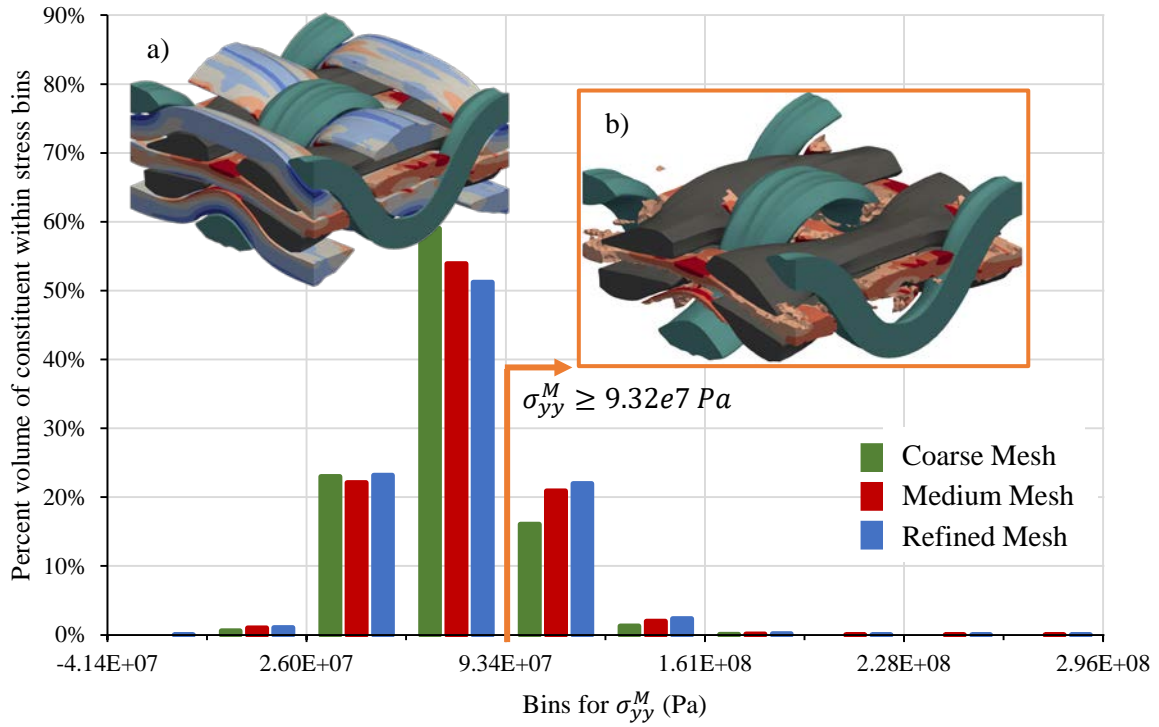
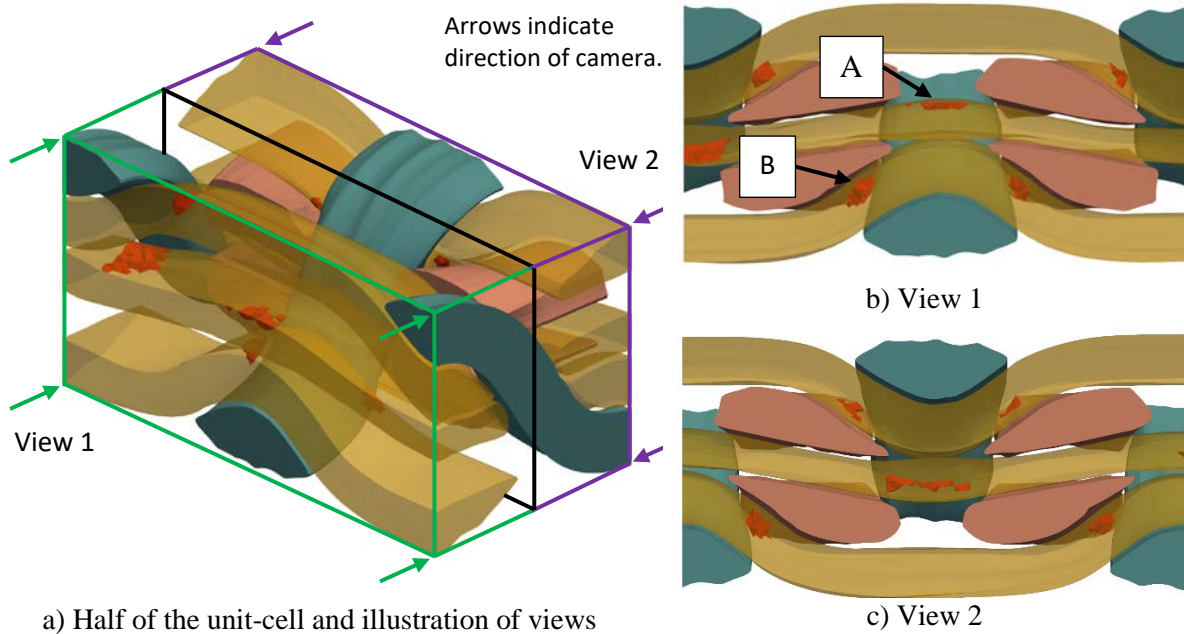


Figure 7. Distribution of  $\sigma_{yy}^M$  within the y-direction tows. For the contour plots, gray indicates a stress near the volume average, while red and blue indicates a value greater or less than the volume average respectively.

The locations of the highest stress concentrations are important, since damage will likely initiate in these locations. To investigate where damage might occur, the material experiencing a value of  $\sigma_{yy}^M$  higher than  $1.27e8$  Pa, which includes the last five bins shown in Figure 7, is shown in Figure 8. Since there is a pattern of locations for these concentrations, Figure 8a only shows half the unit cell and illustrates two key views that show the locations well. The material within the respective bounding boxes in Figure 8a is shown in Figures 8b and 8c, which allows a clear view of the stress concentrations.

Figure 8 shows that even though the middle layer of y-direction tows experiences much higher stresses on average, as shown in Figure 7b, all three layers through the thickness of the textile experience significant stress concentrations. In the top and bottom layers, stress concentrations occur just before and after a y-direction tow crosses an orthogonal tow, near the outermost edges of the tow cross-section. One such location is highlighted as region A in Figure 8b. In the middle layer, stress concentrations occur in the regions where an orthogonal tow reaches its peak or trough. One such location is highlighted as region B in Figure 8b. This leaves a matrix rich region in the center of the textile away from the orthogonal tow, as shown in Figure 8b and 8c, and as a result, the y-direction tows carry more of the load locally in the absence of other fiber reinforced constituents nearby.

For the uniaxial extension considered in this paper, it seems that damage will develop initially within all three layers of y-direction tows. However, the middle layer of y-direction tows will likely experience a more rapid progression of damage since the average stress in the layer is significantly higher than the other two.



a) Half of the unit-cell and illustration of views

Figure 8. Regions of highest  $\sigma_{zz}^M$  (highlighted in red) within the y-direction tows

## 5 CONCLUSIONS

The convergence behavior and stress distribution within the tows were investigated for a 3D orthogonal weave textile composite. This paper used a much higher refinement than what is typically used in the literature, and yet, a mesh convergence was probably not reached. The coarse and medium meshes, which are closer to meshes usually seen in the literature, capture the stress distributions away from the stress concentrations, but the predictions are poor near the stress concentrations. For one of the volume average stresses, the coarse mesh had a 20% error, which is quite large for an averaged quantity. The medium mesh performed better, only differing by 7% or less for the volume average stresses. Further investigation will be needed with very large models will be required to determine fully converge stresses. However, due to the very small volumes of material experiencing the extreme stresses, it is unclear at this point if treating the tows as homogeneous orthotropic materials is valid. Furthermore, it is unclear if artifacts, such as faceted surfaces for the tows, noticeably influence the stress concentrations. Further study will be required to answer these questions.

Using the most refined model, some insight was gained into understanding the location and component of stress that will likely initiate damage. With the tows, the transverse normal stress in the y-direction tows,  $\sigma_{yy}^M$ , was the most severe, indicating matrix cracking within the y-direction tows would likely be the initial damage within the textile. The load was not distributed evenly among the y-direction tows, with the middle layer of tows carrying more load than an exterior layer, but severe concentrations occur in all the layers. Within the X-direction tows, the longitudinal shear stress,  $\sigma_{xz}^M$ , was the most severe, and within the orthogonal tows, the transverse normal stress,  $\sigma_{zz}^M$ , was the most severe. However, the failure modes of these tows are difficult to predict without a progressive damage analysis, since damage in the y-direction tows could significantly change the stress distribution within the other constituents. Due to restrictions on length, this paper only considered the stresses within tows, but the stress distribution within the matrix will be included in future studies. Though there is great potential for the application of 3D textiles, especially in the area of multifunctional composites, this initial study showed that there are significant challenges ahead for accurately predicting the initial stress distributions, much less the eventual failure, of 3D textiles. However, a combination of high-performance computing, novel visualization, and multiscale methods can provide significant insight.

## ACKNOWLEDGEMENTS

This work was supported by the Department of Defense (DoD) through the National Defense Science & Engineering Graduate Fellowship (NDSEG) Program. In addition, the authors acknowledge the Texas A&M Supercomputing Facility (<http://sc.tamu.edu/>) for providing computing resources used in conducting the research reported in this paper.

## REFERENCES

- [1] A. Esser-Kahn, P. Thakre, H. Dong, J. Patrick, V. Vlasko-Vlasov, N. Sottos, J. Moore and S. White, Three-Dimensional Microvascular Fiber-Reinforced Composites, *Advanced Materials*, **23**, 2011, pp. 3654–3658.
- [2] R. Gibson, A review of recent research on mechanics of multifunctional composite materials and structures, *Composite Structures*, **92**, 2010, pp. 2793-2810.
- [3] D. Hartl, G. Huff, H. Pan, L. Smith, R. Bradford, G. Frank and J. Baur, Analysis and Characterization of Structurally Embedded Vascular Antennas Using Liquid Metals, *Proceedings of SPIE Sensors and Smart Structures Technologies for Civil, Mechanical, and Aerospace Systems*, Las Vegas, NV, 2016.
- [4] S. Rawal, D. Barnett and D. Martin, Thermal Management for Multifunctional Structures, *IEEE Transactions on Advanced Packaging*, **22**, 3, 1999, pp. 379-383.
- [5] A. Drach, B. Drach and I. Tsukrov, Processing of fiber architecture data for finite element modeling of 3D woven composites, *Advances in Engineering Software*, **72**, 2014, pp. 18–27.
- [6] S. D. Green, M. Y. Matveev, A. C. Long, D. Ivanov and S. R. Hallett, "Mechanical modelling of 3D woven composites considering realistic unit cell geometry," *Composite Structures*, **118**, 2014, pp. 284-293.
- [7] S. Soghrati, A. R. Najafi, J. H. Lin, K. M. Hughes, S. R. White, N. R. Sottos and P. H. Geubelle, Computational analysis of actively-cooled 3D woven microvascular composites using a stabilized interface-enriched generalized finite element method, *International Journal of Heat and Mass Transfer*, **65**, 2013, pp. 153-164.
- [8] I. Tsukrov, B. Drach, H. Bayraktar and J. Goering, Modeling of Cure-Induced Residual Stresses in 3D Woven Composites of Different Reinforcement Architectures, *Key Engineering Materials*, **577-578**, 2014 pp. 253-256.
- [9] E. V. Iarve, D. H. Mollenhauer, E. G. Zhou, T. Breitzman and T. J. Whitney, "Independent mesh method-based prediction of local and volume average fields in textile composites," *Composites Part A: Applied Science and Manufacturing*, **40**, 12, 2009, pp. 1880-1890.
- [10] H. Si, "TetGen, a Delaunay-Based Quality Tetrahedral Mesh Generator," *ACM Transactions on Mathematical Software*, **41**, 2, 2015.
- [11] I. Tsukrov, M. Giovinazzo, K. Vyshenska, H. Bayraktar, J. Goering and T. Gross, Comparison of two approaches to model cure-induced microcracking in three-dimensional woven composites, *Proceedings of ASME 2012 International Mechanical Engineering Congress & Exposition*, Houston, Texas, 2012.